Anal Bioanal Chem (2016) 408:5109–5124
DOI 10.1007/s00216-015-9014-6

RESEARCH PAPER

Hydrodynamic chromatography coupled to single-particle ICP-MS for the simultaneous characterization of AgNPs and determination of dissolved Ag in plasma and blood of burn patients

Marco Roman[1,2] · **Chiara Rigo**[1] · **Hiram Castillo-Michel**[3] · **Ivan Munivrana**[4] · **Vincenzo Vindigni**[4] · **Ivan Mičetić**[5] · **Federico Benetti**[5] · **Laura Manodori**[5] · **Warren R. L. Cairns**[2]

Received: 10 July 2015 / Revised: 22 August 2015 / Accepted: 26 August 2015 / Published online: 22 September 2015
© Springer-Verlag Berlin Heidelberg 2015

Abstract Silver nanoparticles (AgNPs) are increasingly used in medical devices as innovative antibacterial agents, but no data are currently available on their chemical transformations and fate in vivo in the human body, particularly on their potential to reach the circulatory system. To study the processes involving AgNPs in human plasma and blood, we developed an analytical method based on hydrodynamic chromatography (HDC) coupled to inductively coupled plasma mass spectrometry (ICP-MS) in single-particle detection mode. An innovative algorithm was implemented to deconvolute the signals of dissolved Ag and AgNPs and to extrapolate a multiparametric characterization of the particles in the same chromatogram. From a single injection, the method provides the concentration of dissolved Ag and the distribution of AgNPs in terms of hydrodynamic diameter, mass-derived diameter, number and mass concentration. This analytical approach is robust and suitable to study quantitatively the dynamics and kinetics of AgNPs in complex biological fluids, including processes such as agglomeration, dissolution and formation of protein coronas. The method was applied to study the transformations of AgNP standards and an AgNP-coated dressing in human plasma, supported by micro X-ray fluorescence (μXRF) and micro X-ray absorption near-edge spectroscopy (μXANES) speciation analysis and imaging, and to investigate, for the first time, the possible presence of AgNPs in the blood of three burn patients treated with the same dressing. Together with our previous studies, the results strongly support the hypothesis that the systemic mobilization of the metal after topical administration of AgNPs is driven by their dissolution in situ.

Keywords Silver nanoparticles · Hydrodynamic chromatography · Single-particle ICP-MS · Synchrotron radiation · Burns · Wound dressings

Published in the topical collection *Single-particle-ICP-MS Advances* with guest editors Antonio R. Montoro Bustos and Michael R. Winchester.

✉ Marco Roman
marco.roman@unive.it

[1] Department of Environmental Sciences, Informatics and Statistics (DAIS), Ca' Foscari University of Venice, Via Torino 155, 30172 Venezia Mestre, Italy

[2] Institute for the Dynamics of Environmental Processes (IDPA-CNR), Via Torino 155, 30172 Venezia Mestre, Italy

[3] European Synchrotron Radiation Facility (ESRF), 71 Avenue des Martyrs, 38000 Grenoble, France

[4] Burns Center, Division of Plastic Surgery, University Hospital of Padua, Via Giustiniani 2, 35128 Padua, Italy

[5] European Center for the Sustainable Impact of Nanotechnology (ECSIN), Viale Porta Adige 45, 45100 Rovigo, Italy

Introduction

The multispectral antimicrobial effects of silver (Ag) are known and have been exploited since ancient times, but its use in consumer products and medical devices has proliferated considerably in recent years [1]. Ag-containing devices are widely used in hospitals as adjuvants in the treatment of pathologies where the control of bacterial infections is a key factor for a favourable prognosis [1, 2]. The treatment of burns and chronic skin lesions is one of the most important applications because the local interruption of the blood flow make systemic infection prophylaxes little effective, and topical

administration of Ag-based antimicrobials may therefore be decisive in preventing sepsis [2].

The reactivity of Ag in biological systems is mainly due to the ionic form Ag^+, thanks to its ability to bind organic ligands [3]. In bacteria, such interactions allow the metal to bind to the cell wall, enter the cytoplasm and interfere in key metabolic pathways [4]. However, the high reactivity of Ag^+ in biological systems may also lead to a rapid deactivation and clearance of the metal, mediated, for example, by complexation with serum proteins [5]. Engineered nanoparticles (NPs) provide innovative forms of Ag which can be specifically designed to modulate the release of ions from their surface in a gradual and highly controlled way [6]. Metallic AgNPs have the potential to persist sufficiently for mobilization within biological tissues, and exhibit enhanced affinity for cellular membranes, all of which favours their uptake and delivery to intracellular targets [7]. Several physico-chemical characteristics of AgNPs are a determinant for their dynamics, including size/shape, surface charge and coating, as well as aggregation/agglomeration state. Many properties of the medium also affect their stability in biological systems, including the ionic strength, pH, pE and composition of the organic matter [4]. Complex interactions among these properties of AgNPs and the surrounding media have been conjectured to regulate their transformations in environmental and biological systems [3], but the actual dynamics in situ and in vivo in human tissues remains currently unknown.

A key question is to establish whether AgNPs are able to remain intact for a sufficient length of time and space to reach the bloodstream and undergo systemic distribution. To address this question, adequate analytical tools to detect AgNPs and dissolved Ag in the blood must be developed. Techniques such as transmission electron microscopy (TEM), scanning electron microscopy (SEM) and atomic force microscopy (AFM) enable size characterization of NPs at high resolution [8–10] but cannot provide statistically robust and quantitative data on complex biological fluids with a very low concentration of the metal. Dynamic light scattering (DLS) and static light scattering (SLS) are widely used to characterize NP suspensions but are also inadequate for the analysis of polydisperse particles in complex biological matrices [11, 12]. In addition, none of these techniques provides information on the dissolved fraction of a metal. A powerful technique for quantitative detection of metallic NPs is inductively coupled plasma mass spectrometry (ICP-MS), as it is element specific and highly sensitive, although it has to be coupled to a separation technique to gain a dimensional characterization. A variety of separation techniques, including flow field-flow fractionation (FFF), hydrodynamic chromatography (HDC), reverse-phase (RP) high-performance liquid chromatography (HPLC), ion mobility chromatography (IMC) and micellar electrokinetic chromatography (MEC), have been coupled to ICP-MS for the characterization of AgNPs in standard solutions, plasma and serum, nutraceuticals and a beverage [11, 13–18]. However, all these separation techniques have limitations. Low recoveries are a critical issue in FFF, due to the complex interactions of AgNPs with the membrane, and dissolved ions cannot be detected [11]. RP-HPLC is able to separate AgNPs from ionic Ag, but with poor resolution and low reproducibility for complex biological matrices such as bovine serum [18]. HDC is a robust and versatile method for separating NPs even in complex and heavy matrices, but with poor resolving power. Dissolved ions could also be potentially determined by HDC-ICP-MS, but this application has not yet been explored. MEC-ICP-MS could enable the size-dependent separation of AgNPs and ionic Ag with a higher resolving power but has only been tested on standards [19]. The recent introduction of the single-particle (sp) acquisition mode in ICP-MS has allowed this technique to detect NPs individually, providing quantitative information on their mass distribution and number concentration in solutions [20]. A number of applications have been proposed for the characterization of AgNPs in waters [21–25], but biological matrices remain virtually unexplored, with the exception of enzymatically digested chicken meat [26]. However, spICP-MS does not provide key data for the dynamics of AgNPs in complex systems, including the real diameter, shape, composition and aggregation/agglomeration of the particles, because only their metallic mass can be revealed. The most promising strategy to obtain complete information on NPs in complex media is spICP-MS coupled techniques, but only a few applications have been proposed until now. Online coupling of asymmetric FFF (AF4) to spICP-MS has been explored to study AgNPs in chicken meat [27] and so has HDC-spICP-MS for Ag, Au and polymeric NPs in standard solutions and waters [12, 16, 28]. The determination of dissolved Ag in combination with spICP-MS remains an analytical challenge. Offline separation of the dissolved fraction by ultrafiltration has been proposed [24, 29], but simultaneous online methods would be preferable. Statistical separation of the signals generated by AgNPs and dissolved Ag is possible in spICP-MS by adopting a simple threshold value fixed on the standard deviation of the background [12, 21, 25, 30] or by applying a more complex algorithm based on polygaussian fitting of the frequency distribution [31]. However, such strategies are not suitable for coupled techniques, in which dissolved Ag itself generates a transient signal. Thus, the deconvolution of signals from dissolved Ag and AgNPs in spICP-MS coupled techniques has not yet been attempted.

The goals of the present work were to set up and apply an analytical method based on HDC coupled to spICP-MS for the simultaneous determination of dissolved Ag and the full characterization of AgNPs in human plasma/blood based on an innovative signal deconvolution strategy. An innovative approach combining our method with micro X-ray fluorescence (μXRF) imaging and micro X-ray absorption near-

edge spectroscopy (μXANES) speciation analysis was applied to study in vitro the transformations of AgNPs incubated in the whole human plasma and to investigate, for the first time, the presence of AgNPs in the whole blood of burn patients treated by topical administration of AgNPs under real hospital conditions.

Experimental

Standards, reagents and samples

An Ag ICP-MS grade 1000 ng mL^{-1} standard solution (certificated, NIST teachable) was obtained from Ultra Scientific (Bologna, Italy) and used to calibrate the total Ag measurements. Commercial standards of AgNPs purchased from Sigma-Aldrich were used for method development, calibrations and incubation experiments. The standards consisted of monodisperse metallic NPs with nominal diameters of 10, 20, 40, 60 and 100 nm (provided uncertainty ±4 nm), mass concentration 20±0.5 μg mL^{-1}, suspended in aqueous solution and stabilized with sodium citrate. The standards were characterized by TEM resulting in a size distribution compatible with the values provided by the manufacturer, and spherical shape. The z-potential of the mother dispersions was measured confirming their good stability (≤40 mV). Details on the experimental procedures for characterization of the standards, representative TEM images and a summary of their size/shape parameters and z-potential can be found in the Appendix. The measured size of the standards was used for all calculations, but for simplicity, we refer to their nominal diameter throughout this paper. The exact mass concentration as total Ag of the mother dispersions was also measured by ICP-MS, and the number concentration was calculated based on the experimental mode of the size distribution.

The commercial dressing Acticoat Flex3™ (Smith & Nephew) was used for the in vitro incubations and the in vivo treatment of burn patients as reported elsewhere [1]. The mobile phase for chromatography was prepared using sodium dodecyl sulfate (SDS), HNa_2PO_4 dihydrate and IGEPAL® CA-630 nonionic detergent in the following concentrations: SDS 0.05 % *v*/*v*, HNa_2PO_4 0.002 M and IGEPAL 0.1 % *v*/*v* at pH 7.4. A water solution containing tetramethylammonium hydroxide (TMAH) 0.1 % *v*/*v*, NH_4OH 2.8 % *w*/*w* and Triton™ X-100 0.1 % *v*/*v* was used to dilute by 20-fold the whole blood for total Ag determination by ICP-MS. Reduced L-glutathione (GSH)- and human serum albumin (HSA)-lyophilized powders were used for incubation experiments. All incubations were carried out in a normal laboratory environment at 37 °C in a thermostated bath, under constant gentle shaking in the dark. The preparation steps for standards and samples were carried out in a class 1000 clean room environment under a class 100 laminar flow bench.

Whole human plasma for incubations and control whole blood were provided by distinct volunteers and were collected at the University Hospital of Padua. Four samples of whole blood were provided by the bio-bank of the same hospital and were collected from three adult patients treated in the same hospital, at the burns centre, following the current protocols without any additional invasive procedure. The patients did not present any pathology other than the burn. All samples were collected and stored in agreement with the guidelines of the University Hospital of Padua, and informed consent of the patients was obtained according to the Helsinki Declaration. The blood was collected in purple-tip vials (K2–3EDTA) in order to prevent coagulation, was immediately frozen to lyse the red blood cells and was stored frozen until analysis.

Instrumentation

The chromatographic system consisted of an Agilent Technologies (Tokyo, Japan) 1200 series HPLC pump fitted with an HDC 5-300 Type 1 column (linearity range 5 to 300 nm) from the same supplier. Sample injections were performed manually using a 100-μL loop and an inert Rheodyne injection valve. The elution was performed in isocratic mode at a flow rate of 1.0 mL min^{-1}. An ICP-MS detector (model 7500cx) from Agilent Technologies was coupled online to the chromatographic system using a PolyPro nebulizer mounted on a double-pass Scott spray chamber thermostated at 2 °C. The instrument operated at 1500 W RF power with a carrier gas flow rate of 1.1 mL min^{-1} and make-up gas flow rate of 0.1 mL min^{-1}. The lens voltages were tuned daily for best sensitivity using a 1 ng mL^{-1} solution of Ag. In order to minimize the matrix effects, robust plasma conditions were achieved by keeping oxides and double charges rates below 2 % based on the response of a Ce 1 ng mL^{-1} solution and using 8 mm of the sample depth. Acquisition was carried out by monitoring both the isotopes of Ag (*m*/*z* 107 and 109) with a dwell time of 5 ms. Automatic correction for the dead time was adopted, and the parameter was estimated as reported elsewhere [32]. A settling time of 2 ms was automatically selected by the instrument and was taken into account to correct the calibration of NPs number concentration, as reported below.

Synchrotron radiation μXRF and Ag L_{III}-edge μXANES measurements were performed using the scanning transmission X-ray microscope of beamline ID21 at the European Synchrotron Radiation Facility (ESRF, Grenoble, France). Details on standards/sample preparation, instrumental parameters and data elaboration for μXRF and μXANES are provided as supporting information.

Data elaboration

Data treatment for HDC-spICP-MS was carried out using a home-made program written in Fortran language and run using the compiler Compaq Visual Fortran (Compaq Computer Corporation). The program reads the ICP-MS raw data file directly and provides a number of output files including overall statistics and matrices. The latter were directly imported in Surfer 11 (Golden Software) for graphical elaboration of the contour plots (3D chromatograms). Excel spreadsheets (Microsoft), OriginPro 8.5 (OriginLab) and Statistica 10 (StatSoft) were used for additional calculations and graphical elaboration. PyMca [33] and Athena [34] software were used to elaborate the μXRF and μXANES data.

Results and discussion

Implementation of data analysis

Dwell time and data pre-processing

The limit of detection (LOD) in spICP-MS has two possible interpretations: as the lowest detectable particle size (LOD_S^{NP}) and the lowest detectable particle number (LOD_N^{NP}). Measuring simultaneously, the dissolved Ag introduces also a third definition, which is the lowest detectable concentration of this fraction (LOD_C^D). The choice of the dwell time is the key to determine all these parameters in samples where both NPs and dissolved Ag are present and the overall statistical reliability of the results in spICP-MS. Individual NPs in ICP-MS generate transient signals with a temporal width of 0.3–0.5 ms [35]. Recent instrumentation allows setting the dwell time within the microsecond range, so that single events can be described by multiple data points. This results in a significant reduction of the background, a decreased LOD_S^{NP} and an improved range of number concentration [36]. However, the same increase in the signal-to-background ratio is expected to make the determination of the dissolved Ag by statistical deconvolution within the same analysis more difficult, increasing the LOD_C^D. Moreover, with microsecond dwell times, the probability to observe split of events between adjacent time windows must be taken into account [30] and the electronic and computational load due to data size can be potentially problematic when applied to coupled techniques, where the acquisition lasts for tens of minutes. Conversely, conventional millisecond dwell time leads to higher LOD_S^{NP} and requires higher dilution of the samples to avoid detecting multiple events within the same time window [30], but it is more suited for performing the simultaneous determination of dissolved Ag and using coupled instrumental approaches. According to other authors, a dwell time in the range of 3–5 ms is adequate to achieve good quality data in our context [37].

The minimum dwell time that can be set on our instrument for the acquisition of a single *m*/*z* is 10 ms, but a dwell time of 5 ms can be chosen by monitoring both masses of Ag. This required a data pre-processing step for normalization of the two signals to the relative natural abundance of each respective isotope, before merging them into a single chromatogram. Given the proximity of the two abundances (0.518 for ^{107}Ag and 0.482 for ^{109}Ag), the difference in signal intensity for the two masses is negligible at low counting rates but was, nevertheless, taken into account when applying the threshold in the following deconvolution step. In addition, the acquisition of two masses introduces a settling time, which slightly affects the number of detected particles (see the "Calibrations and elaboration of the 3D NPs final chromatograms" section).

Deconvolution of the signals

The expected forms of dissolved Ag in plasma (protein complexes) have hydrodynamic diameters smaller than the LOD_S^{NP} (see the "Calibrations and elaboration of the 3D NPs final chromatograms" section) and close to the lower limit of separation range. Given also the poor resolving power of HDC, their peak cannot be chromatographically resolved from those of ~20-nm particles, thus making deconvolution a necessary operation. In this work, the statistical deconvolution of the signals from dissolved Ag species and AgNPs was based on a nonparametric statistical test applied to each data point of the chromatogram as it was sequentially scanned. The intensity value of each point was compared to that of its two adjacent neighbours, and their difference was calculated. If at least one of the two differences overcame a threshold value given by the maximum expected difference between any data generated by dissolved Ag, the hypothesis of the point being associated to dissolved forms was rejected. For each pair of points to be compared, the relative threshold value was specifically calculated as a negative exponential function of the lower of the two intensities. The function was externally calibrated on the chromatogram of a single standard of dissolved Ag with a relatively high concentration (500 pg mL^{-1}) using the following procedure. The chromatogram was divided into consecutive windows of 2 s in width, in which the signal was assumed to be stationary. For each window, the empirical distribution of the data was calculated to extract the 1st-to-99th interpercentile range. The range was plotted against the average value within the same window as shown in Fig. 1a. The interpercentile range can be interpreted as the maximum difference in signal intensity between two data points generated by dissolved Ag at a 98 % confidence level and was adopted here as the threshold value to discriminate the signals. The vector of points for which the hypothesis of being generated by dissolved Ag was rejected constituted the NPs extracted chromatogram.

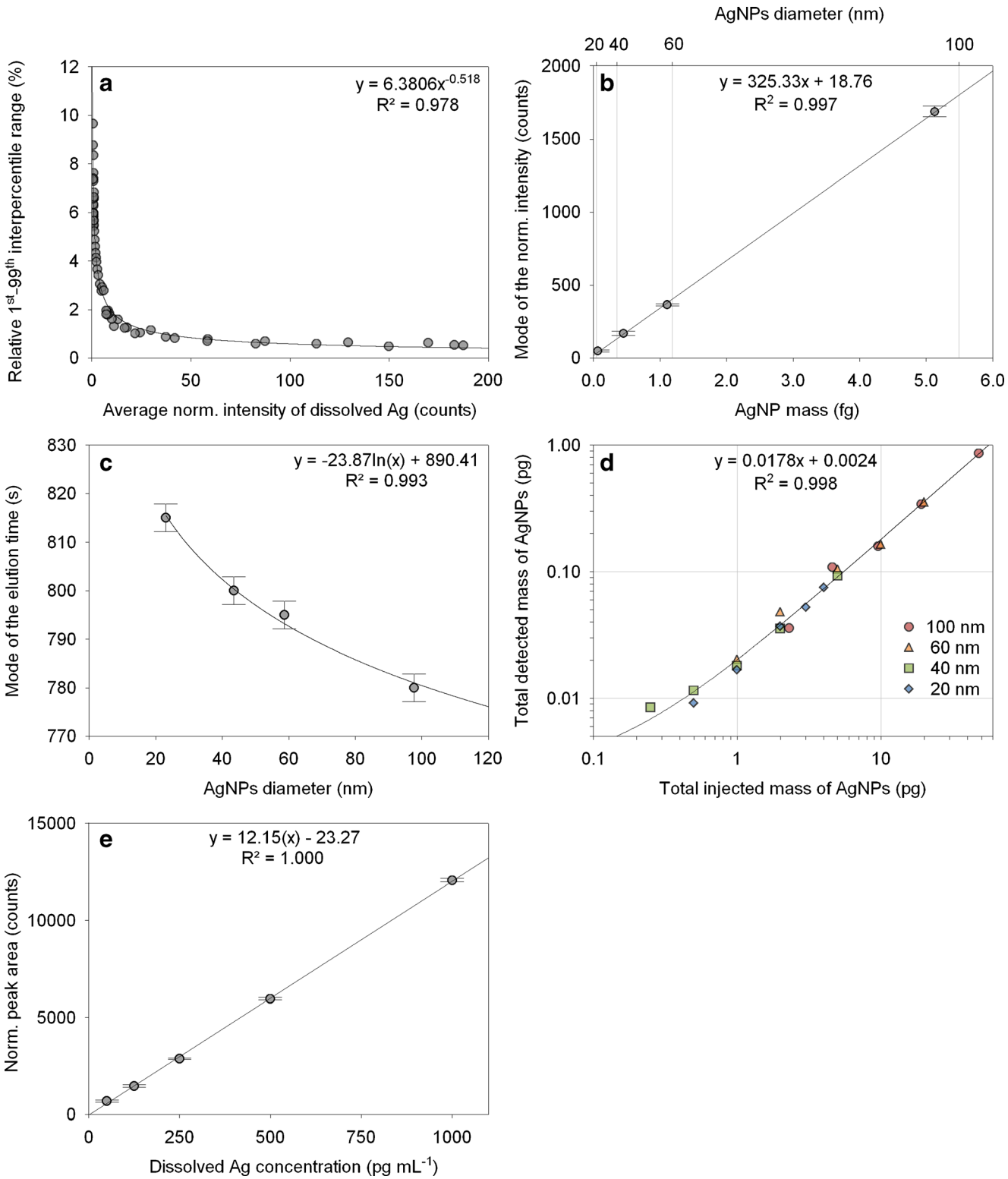

Fig. 1 External calibrations applied to elaborate the HDC-spICP-MS chromatograms. **a** The 1st–99th interpercentile range of the normalized signal intensity relative to the average value calculated for dissolved Ag (500 pg mL^{-1}) within 2 s time windows, plotted against the corresponding average intensity. The range was adopted as the variable threshold for deconvolution of dissolved Ag and AgNPs signals. **b** Calibration of the normalized signal intensity as a function of the mass of AgNP standards with 20, 40, 60 and 100 nm nominal diameter (hypothesis of purely metallic spherical particles, n=3). **c** Calibration of the elution time as a function of the diameter of AgNP standards with 20, 40, 60 and 100 nm nominal diameter (n=3). **d** Calculation of the AgNP detection efficiency as slope of the regression line, detected mass vs. injected mass (bilog scale). The injected standards were 20 nm (5, 10, 20, 30 and 40 pg), 40 nm (2.5, 5, 10, 20 and 50 pg), 60 nm (10, 20, 50, 100 and 200 pg) and 100 nm (25, 50, 100, 200 and 500 pg). **e** Calibration of the peak area for dissolved Ag (n=3)

Elaboration of the 3D NPs raw chromatogram

The NPs chromatogram was firstly treated by converting the normalized signal intensities into their cube square. This step was necessary to obtain final chromatograms in which the mass-derived diameter is represented on a scale with uniform resolution. In a second step, the dimensions of elution time and normalized signal intensity were gridded into windows of selected width according to the procedure proposed by Pergantis et al. [28]. The width of the intensity windows was fixed at 0.6266 normalized counts$^{1/3}$, resulting in a resolution of 6.5 nm for the mass-derived diameter after calibration. The width of the elution time windows was fixed at 5 s in order to contain 714 data points to guarantee statistical representativity. After gridding, the number of events detected within each window was counted and a raw 3D chromatogram was yielded as a three-column matrix consisting of the central values of the elution time (x-axis), the normalized events' intensity (y-axis) and the number of detected events (z-axis) for each window.

Calibrations and elaboration of the 3D NPs final chromatograms

Besides the threshold function, other external calibrations based on the injection of monodisperse NPs standards were necessary to convert the normalized signal intensity into mass-derived diameter and the elution time into hydrodynamic diameter. Standard suspensions with a nominal size of 20, 40, 60 and 100 nm and variable concentration were injected to calibrate these two parameters as done by Pergantis et al. [28]. For each standard, the mode of the 3D raw chromatogram provided the data to be included in the calibration curves, which are shown in Fig. 1b, c. A LOD_S^{NP} of 16 nm was calculated as three times the standard error of the intercept of the mass calibration curve. This value is in agreement with the range of those estimated by other authors both theoretically and experimentally (in water samples) using spICP-MS [22]. The extrapolation of the number concentration of AgNPs in a sample required estimating separately their transport efficiency through the nebulization system. Adapting the formula by Pace et al. [38], the overall number of detected particles n_r of radius r, using the hypothesis of purely metallic and spherical particles, can be expressed as

$$n_r = \eta \cdot \frac{c_r^m}{\frac{4}{3}\pi r^3 \rho} \cdot v \cdot \frac{t_i}{t_s + t_i} \quad (1)$$

where η is the transport efficiency (independent by the radius), c_r^m is the mass concentration of the NPs (pg mL^{-1}), v is the injection volume (mL), ρ is the density of Ag in pg nm^{-3} = $1.049 \cdot 10^{-8}$, t_i is the integration time, and t_s is the settling time.

The transport efficiency can be estimated by analyzing a series of standards of any radius at different known mass concentrations, calculated as the slope of the regression line in Eq. 1. However, one should note that even if it is approximately monodisperse, a standard suspension still has a characteristic size distribution which may be not perfectly symmetric, particularly for the size ranges close to the LOD_S^{NP}, so that simple counting the overall number of detected particles would introduce a bias. In order to overcome this potential problem, we used the calibration of mass-derived diameter to convert the number of detected particles into a mass for each window of the raw chromatogram. Summing the mass of all windows provided the total detected mass of Ag, to be used in place of n_r for efficiency estimation. The method was tested on four nominal particle sizes, as shown in Fig. 1d. Consistent with the independence of η from the particles' size, an average value of 1.78±0.07 % was obtained for the four calibrations. If a minimum number of three detected particles are arbitrarily adopted as the statistical threshold to verify their presence, taking into account the transport efficiency, settling time and injection volume, a LOD_N^{NP} of ~2300 particles mL^{-1} is achieved. This threshold can be indifferently adopted for all particles or for specific size classes. Finally, a calibration was also required for the dissolved Ag fraction by injecting standards of ionic Ag with variable concentration as shown in Fig. 1e, obtaining a LOD_C^D of 13 pg mL^{-1}.

All calibrations reported above allowed us to convert the data of the 3D NPs raw chromatogram for each sample into a final chromatogram representing the experimental distribution of NPs in terms of number concentration or mass concentration depending on the hydrodynamic diameter and mass-derived diameter.

Stability of the AgNPs in the mother standards and in mobile phase

The mother citrate-stabilized dispersions were stored at 4 °C, and no significant changes in their size distribution were noticed after more than 1 year (as observed by TEM). In addition, no peaks of dissolved Ag were detected by HDC-ICP-MS when injecting single standards freshly diluted in mobile phase for calibration within the same time span. The temporal stability of AgNP standards in the mobile phase below the nanogram per millilitre level was also checked. Despite the appearance of small peaks of dissolved Ag was observed after leaving the vials exposed to light and room temperature up to 24 h, the corresponding concentration was below the LOD_C^D for all particle sizes. Nevertheless, in order to avoid any potential alteration of the dynamics of AgNPs due to interaction with the mobile phase, all standards for calibration were always prepared freshly from the mother dispersion and immediately injected, all samples were analyzed immediately after

preparation, and replicates were obtained from independent preparations rather than from repeated injections.

Dynamics of AgNPs incubated in human plasma

The developed method was used to study the dynamics of AgNPs in human plasma. Standards with nominal diameters of 20, 40, 60 and 100 nm were mixed in whole plasma at concentrations of 10, 16, 37 and 100 ng mL^{-1}, respectively, sonicated for 1 min and then incubated for 2 h. After incubation, the sample was diluted 20-fold in the mobile phase and directly injected without further sonication. A control sample was prepared by diluting the AgNP mixture in the mobile phase at the same final concentration, followed by sonication for 1 min and direct injection. Figure 2 shows the final 3D chromatograms obtained for the control and plasma incubated mixtures. A number of significant changes were observed in the distributions of NPs after 2 h of incubation in plasma: (i) a slight general decrease in the mass-derived diameter, (ii) a significant decrease in the number and mass concentration of the NPs and (iii) a generalized shift in the distribution towards the higher hydrodynamic diameters of 10–20 nm. While the first two effects can be ascribed to a partial dissolution of the NPs, the increased hydrodynamic diameter is compatible with two possible phenomena: the agglomeration of NPs and the formation of a protein corona onto their surface. The agglomeration of uncapped NPs is a feasible process in plasma, particularly due to the relatively high ionic strength of the medium [3]. We did not observe the appearance of new modes in the mass-derived diameter corresponding to multiples of the nominal diameters of 40, 60 and 100 nm. However, agglomeration effects cannot be excluded for the 20-nm particles due to the theoretical superimposition of the multiples of their mass on the modes of the other standards. Conversely, the formation of a protein corona is a plausible generalized process, particularly due to the interaction of thiol groups in amino acids with the charged surface of AgNPs in a medium with a high ionic strength [39, 40].

In order depict the temporal dependence of the dynamics of AgNPs in human plasma, the standard suspension with a 100 nm size was selected for further incubation experiments. An aliquot of the mother monodisperse suspension (20 μg mL^{-1}) was sonicated for 1 min and then mixed 1:1 with plasma and incubated for 24 h. At time steps of 2, 4, 6, 8, 16 and 24 h, aliquots of the solution were collected, diluted 10,000-fold in the mobile phase and analyzed immediately. Figure 3a shows that the dissolution of AgNPs is not linearly time dependent on an hourly scale in a closed system. The most significant change was observed between the 4- and 8-h incubations, with a decrease in the molar fraction of Ag present in the original form of NPs, corresponding to the appearance and increase of the dissolved fraction. Between 16 and 24 h, the molar fractions seem to reach equilibrium. The precision of detection efficiency (~4 % of relative error, see the "Implementation of data analysis" section), which affects the estimated number concentration, is the dominant source of uncertainty for AgNPs molar fraction. The calibration of dissolved Ag is more reproducible because the relative error of the slope of its calibration curve (Fig. 1e) is 1 %. The mass-derived diameter of the particles exhibits a substantial linear decrease from 100 to 80 nm in 24 h (Fig. 3b), confirming the partial dissolution of the individual particles. In this case, the standard deviation among replicates is zero because their differences are smaller than the width of the signal intensity windows adopted for gridding (see the "Elaboration of the 3D NPs raw chromatogram" section). Thus, for each estimated diameter (d), the width of the gridding windows ±6.5/d % can be considered as the maximum theoretical uncertainty and was taken to represent the whiskers in Fig. 3b.

Speciation analyses by μXANES were carried out on analogously incubated samples. Standards of AgNPs with a 10 nm size (20 μg mL^{-1}) and ionic Ag solution (nitrate, 10 μg mL^{-1} as Ag) were incubated in a water solution containing HSA (~0.5 mg mL^{-1}) and in whole plasma. After 2 h, a drop of each solution was freeze-dried between Ultralene® windows and was directly analyzed by μXANES. Representative spectra for each of the incubated standards and pure species of Ag, as shown in Fig. 4a, b, allowed us to identify the chemical forms of Ag after incubation and their relative molar fractions estimated by linear combination fitting (LCF), as reported in Table 1. The μXANES analysis showed that after 2 h of incubation in HSA, the Ag^+ ions were mostly complexed by thiols (represented by the AgGSH bound). Conversely, AgNPs remained intact almost quantitatively, even if Ag-thiols were also detectable. This confirms that the formation of a protein corona on the surface of AgNPs has a major inhibiting effect on their dissolution in the short term. Differently, in whole plasma, the early dynamics of Ag was dominated by chlorides, with formation of insoluble AgCl from free Ag^+ and significant agglomeration of the AgNPs, as marked by the high weight of the metallic Ag foil spectrum obtained by LCF.

Dynamics of AgNP agglomerates released from a dressing incubated in human plasma

The 2-h incubation experiment in whole plasma was carried out also using the intact Acticoat Flex3™ dressing. The dressing consists of a net of polyethylene fibres, individually and uniformly coated with a layer of uncapped AgNPs of 10 nm in size; other characteristics of the product can be found elsewhere [32]. Previous experiments showed that the dressing releases AgNPs as agglomerates with widely variable size in vitro in the human serum substitute [41] and agglomerates were also detected in the fibroblasts of burn patients after 7 days of treatment [1]. In this experiment, 2.45 mg of the

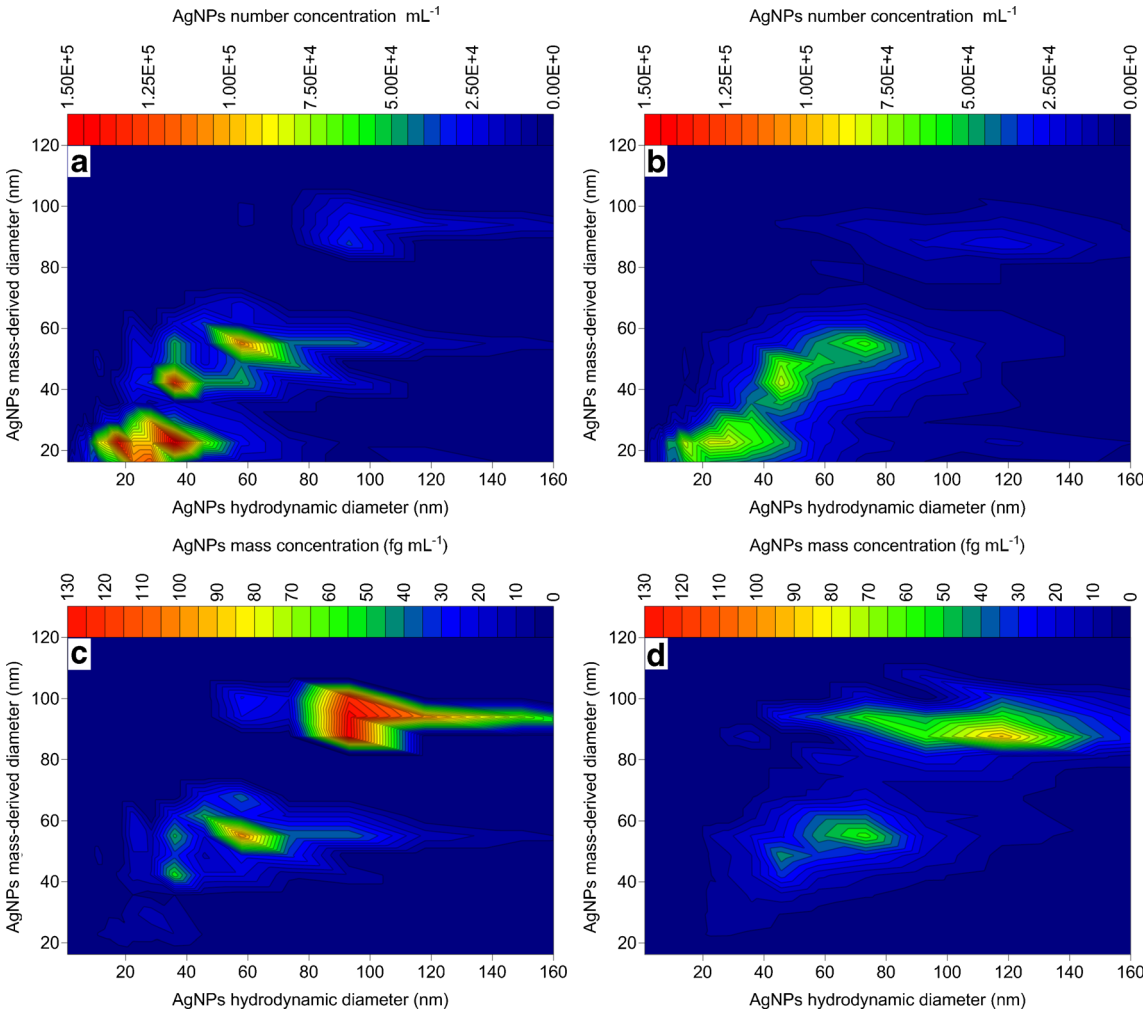

Fig. 2 Three-dimensional contour plot chromatograms of AgNPs obtained for a mixture of 20, 40, 60 and 100 nm standards diluted in mobile phase (**a**, **b**) and the same mixture incubated for 2 h in plasma (**c**, **d**)

dressing (0.32 mg as Ag) was dipped into 1 mL of the whole plasma and sonicated for 10 min to accelerate the release of AgNPs as individual particles or small agglomerates. After 2 h of incubation, the plasma was centrifuged at 3000 rpm for 10 min in order to remove the fibres, cloth debris and micrometric agglomerates of AgNPs and then an aliquot was diluted 100-fold in the mobile phase and directly injected into the chromatographic system. The 3D chromatograms in Fig. 5a, b show a few particles with size >16 nm, corresponding to small agglomerates of two to five NPs of 10 nm in size. Significantly higher hydrodynamic diameters, with respect to the mass-derived diameter, were also observed. The latter effect supports the hypothesis that the observed particles are small (non-spherical) agglomerates, and is also compatible

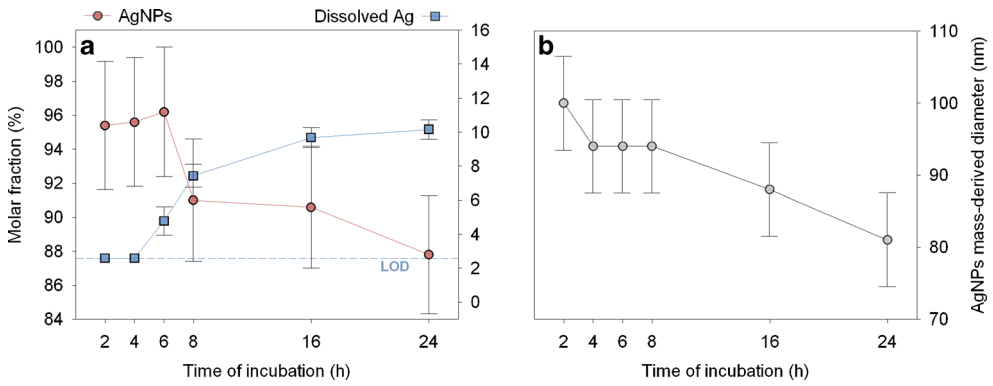

Fig. 3 **a** Temporal variation of the molar fractions of AgNPs and dissolved Ag in plasma after incubation of a 100 nm standard from 2 to 24 h, average±standard deviation, n=3. **b** Temporal variation of the mode of the AgNPs mass-derived distribution in the same incubated standard, average±theoretical uncertainty, n=3

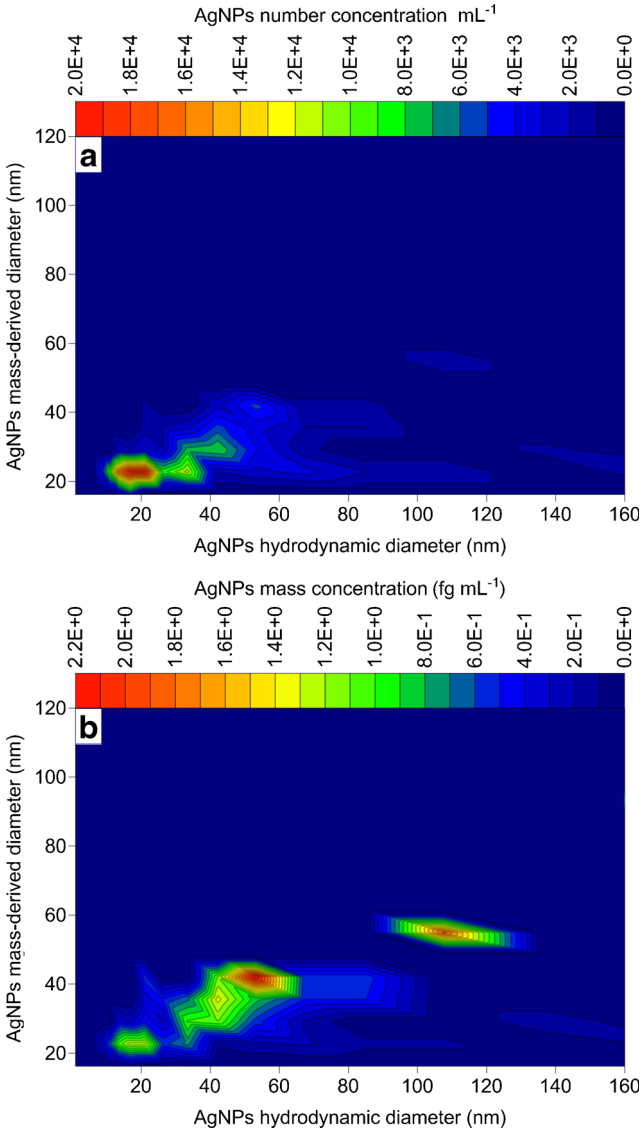

Fig. 4 Three-dimensional contour plot chromatograms of AgNPs after incubation of the Acticoat Flex3™ dressing in plasma for 2 h

with additional protein capping effects. The dissolved Ag fraction resulted to lower than the LOD_C^D.

A 20-μL aliquot of the same sample after incubation was collected before centrifugation, freeze-dried and analyzed by μXRF and μXANES. Preliminary μXRF mapping of the sample allowed us to detect a number of micrometric agglomerates of AgNPs or fragments of the dressing. A region surrounding one of the particles was selected, and the distribution of Ag, Cl and S was mapped as shown in Fig. 6a. A characteristic non-uniform accumulation of Cl was observed at the border of the Ag particle, while S was uniformly distributed in the surrounding medium. μXANES spectra were collected in the same region for each pixel to be individually elaborated by LCF in order to extract a coarse estimation of the molar fraction of the three main expected species: intact AgNPs, AgCl and Ag-thiols. The resulting μXANES map is shown in

Table 1 Semiquantitative speciation of Ag in the dressing Acticoat Flex3™, AgNPs of 10 nm in size and ionic Ag incubated in solutions containing HSA or in whole human plasma for 2 h

Experiment	Species	Molar fraction %
10 nm Ag^0NPs in plasma	Ag^0 foil	66
	10 nm Ag^0NPs	28
	Other	6
Ag^+ in plasma	AgCl	63
	Other (×2)	37
10 nm Ag^0NPs in HSA	10 nm Ag^0NPs	93
	AgGSH	7
Ag^+ in HSA	AgGSH	67
	Other	33
Acticoat Flex3™	10 nm Ag^0NPs	66
	Ag^0 foil	34
Acticoat Flex3™ in plasma	AgCl	59
	10 nm Ag^0NPs	32
	AgGSH	10

Data were obtained by LCF of the μXANES spectra; the AgGSH standard is a representative of Ag-thiol bonds

Fig. 6b. Although total Ag and Cl presented widely different distributions, a relatively uniform distribution of the Ag species was observed, consistent with the participation of the whole surface of the AgNPs agglomerate in the chemical dynamics of the metal. The average molar distribution of the species within the entire region was 49 % AgCl, 22 % AgNPs and 20 % Ag-thiols (9 % unidentified species). The overall distribution was also estimated by firstly merging all the spectra within the region and then performing the LCF on the pooled spectrum. This procedure allowed us to weight the contribution of each pixel on the base of the total Ag level and provided the following values: 53 % AgCl, 31 % AgNPs and 15 % Ag-thiols. Compatibly with Fig. 6b, the slight variations with respect to the previous estimation are consistent with a major localization of AgCl and AgNPs in the regions with elevated Ag level while Ag-thiols are mainly present in the peripheral areas. The assignment of previously unidentified species could also have affected the latter values. The co-presence and relative proportion of the three species reveal that the dynamics of AgNPs in plasma involves integrated and complex processes. Free Ag ions are expected to be a negligible fraction in biological systems due to the high formation constant for chloride and thiol bonds [3, 42], so that dissolution and formation of complexes may take place directly on the surface of the AgNPs as an integrated process. Properties of the medium such as its general composition, concentration of chloride and pH and kinetics of complexation influence the dynamics. Although protein thiols should be thermodynamically favoured for Ag binding in plasma with respect to

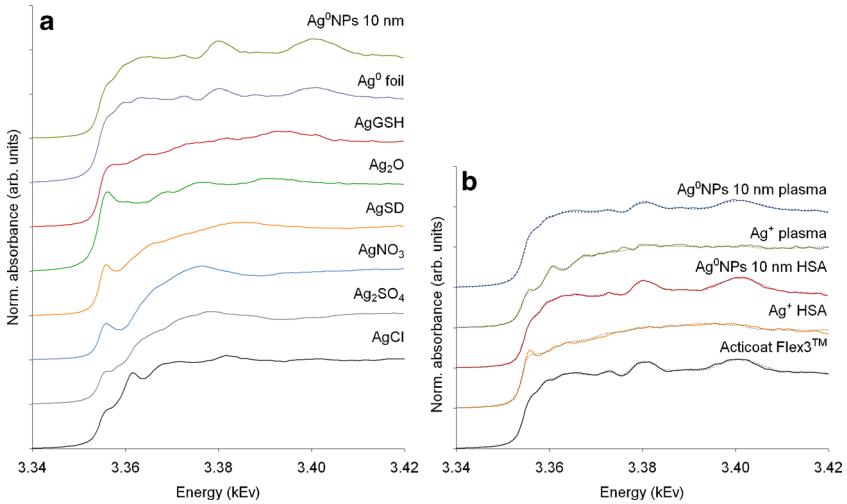

Fig. 5 **a** μXANES spectra of pure standards of Ag species. **b** μXANES spectra of the Acticoat Flex3™ intact dressing and 10 nm AgNPs and ionic Ag incubated in a solution containing HSA or in whole human plasma. The original spectra of the incubated standards are superimposed to their best fitting (*dotted lines*) obtained by LCF using the pure standards as the input variables. The fitting parameters (molar fractions) are reported in Table 1. AgGSH is a representative of the Ag-thiol bounds

chlorides [3, 6], our data support the hypothesis that the latter has a kinetic advantage when interacting with Ag ions directly on the charged surface of the bare NPs, leading to an early effect of partial dissolution and, possibly, agglomeration of the smallest NPs. Still, protein thiols may co-participate to this dynamics by enclosing the particles and superficial chlorides, inhibiting further interactions with the medium, the removal of AgCl from the surface and further agglomeration effects. Given the affinity of thiols for Ag, subsequent displacement of the metal from the chlorides is likely, resulting in its final mobilization. In agreement with Liu et al. [3], thiol binding appears to be the limiting process in regulating the dissolution of AgNPs in plasma, and the mediator for systemic distribution of the metal, but our findings suggest that kinetic factors play a crucial role in this complex dynamics.

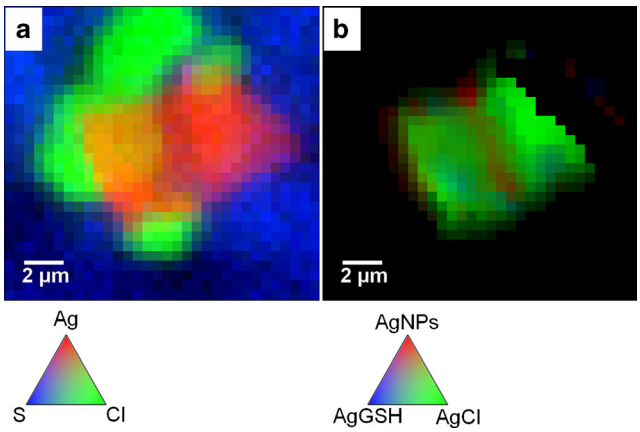

Fig. 6 **a** μXRF map of the distribution of Ag, Cl and S in the region surrounding a micrometric agglomerate of AgNPs released by Acticoat Flex3™ after 2 h of incubation in plasma. *Scale* is linear in cps with independent full-scale values. **b** μXANES map of Ag speciation in the same region. *Scale* is linear in cps with the same full-scale value for all species. AgGSH is a representative of the Ag-thiol bounds

Whole blood from burn patients treated with a AgNP-containing dressing

In addition to the temporal dynamics of the chemical transformations of AgNPs, the particles could also undergo simultaneous mobilization through the tissues, with consequent change in the properties of the surrounding medium. The formation of a protein corona is probably the main favouring factor for the cellular uptake on AgNPs [40], which has been observed in human skin both in vitro and in vivo in burn patients [1]. However, the few available experimental data suggest that the metal has a poor capability to penetrate the skin in depth, even if penetration may be enhanced in damaged tissue [1, 43].

In order to evaluate the actual potential of AgNPs to reach the bloodstream before dissolution, we used HDC-spICP-MS to analyze the four whole blood samples collected from three adult patients (A–C) treated for mid-thickness skin burns with a single application of the dressing. The main clinical information is summarized in Table 2. The patients had a comparable percentage of burnt body surface, which represents the wound area exposed to AgNPs. Three blood samples were collected from distinct patients 3 days after the application, and an additional sample was collected from patient A after 6 days of treatment. Compatibly with our previous estimations that the dose of Ag released by the dressing into the patient's tissues in vivo would be elevated [32], a significant level of total circulating Ag was observed in all patients after 3 days of application of the dressing (Table 2). The values ranged between ~30 and 80 ng mL^{-1} and were more than 2 orders of magnitude higher than the baseline level in an unexposed population [44] and slightly lower than those observed in the serum of paediatric burn patients treated with the same dressing (average 114 ng mL^{-1}) [45]. Differently from the latter cited work, we did not observe any apparent correlation between blood Ag and the percentage of burnt body area, and

Table 2 Main clinical information on the adult burn patients treated with Acticoat Flex3™ and concentration of total Ag and dissolved Ag fraction in their whole blood

	Patient A		Patient B	Patient C
Burn location	Torso+left arm		Torso	Torso+arms
Burnt body surface, %	22		27	30
Degree	II		II	II
Dermabrasion	Yes		Yes	Yes
Treatment duration, days	3	6	3	3
Total Ag in blood, ng mL^{-1}	46.6	48.9	83.1	36.9
Total Ag in the centrifuged blood, ng mL^{-1} (recovery %)	44.5 (96)	46.7 (96)	81.4 (98)	28.1 (76)
Dilution factor	100	100	250	75
Dissolved Ag in the centrifuged blood, ng mL^{-1} (molar fraction %)	37.9 (85)	41.6 (89)	83.9 (103)	28.0 (100)

just a slight increase in Ag was noticed after three additional days of application for patient A.

An aliquot of the blood was then centrifuged at 3000 rpm for 10 min to remove the cell debris in order to avoid clogging the chromatographic system. The supernatant was recovered and analyzed for total Ag. The average recovery of total Ag after centrifugation was ≥96 % for all the samples except patient C (76 %), and a minimal loss of Ag due to co-precipitation was therefore assumed for most cases. The possibly co-precipitated Ag can be ascribed to its association to cellular debris and large biomolecules whose size exceeds the effective separation range of the HDC system. Based on the total concentration of Ag, the centrifuged samples were diluted in the mobile phase according to specific dilution factors (see Table 2), optimized to obtain the same final concentration of ~400 pg mL^{-1} of Ag. This target value was selected from preliminary tests as the optimum concentration for detecting a significant number of AgNPs with a mass-derived size close to the LOD_S^{NP} under the hypothesis that they were present as a significant molar fraction of Ag (>10 %).

We did not detect any significant event associated to AgNP agglomerates >16 nm in the four blood samples (chromatograms are not shown). Conversely, from the chromatograms of dissolved Ag as shown in Fig. 7, an average molar fraction of 94±9 % was estimated for the dissolved species (see Table 2), which is not statistically different from the total level of the metal.

Considering that (i) our previous studies have shown that in burn patients treated with Acticoat Flex3™, AgNPs are released as agglomerates and maintain this form even in the tissue; (ii) a poor dermal penetration of PVP-coated AgNPs, restricted to small (<30 nm) particles in damaged skin, was observed in vitro [43]; and (iii) we documented here that small AgNPs exhibit both agglomeration and partial dissolution effects at an hourly time scale in plasma; the results of blood analysis strongly support the hypothesis that the systemic mobilization of Ag is driven by the in situ dissolution of NPs in the skin. The first medium entering in contact with the AgNPs released by the dressing onto the wound bed is the exudate, whose composition is similar to the serum. This medium is the major candidate to host the in situ transformations of AgNPs, where dissolution may be also enhanced by the lower pH (5.7), typical of the inflammatory phase in wounds [46]. It is also likely that the reduced blood circulation in burns further inhibits the dispersion of AgNPs. However, let us keep in mind that the specific local characteristics of the wound may dramatically affect the release of AgNPs from the dressing and the composition/production/turnover of the exudate. This can lead to significantly different AgNPs dynamics at a local level, resulting in the possible penetration of agglomerates into the shallow tissue layers. Photochemical reduction of Ag complexes with formation of secondary Ag/S/Se particles can also occur in the skin [3]. We previously observed a few electron-dense particles in skin biopsies after application of the dressing, which are potentially representative of photoprecipitation [1]. However, this phenomenon appears to be limited to the most severe lesions, which require long-term treatments and replacement of the dressing, leading to exposure to light and an increased Ag dose.

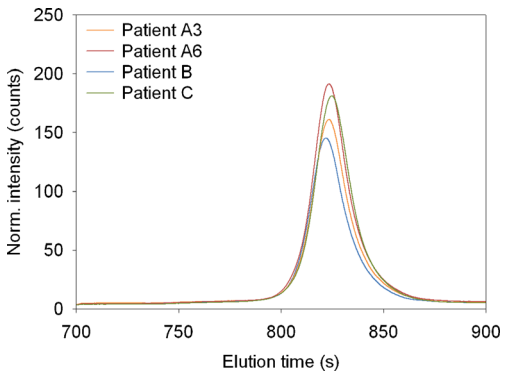

Fig. 7 Deconvoluted chromatograms of dissolved Ag in the whole blood of burn patients obtained by HDC-spICP-MS. The blood was collected 3 days (patients A3, B and C) and 6 days (patient A6) after the application of the Acticoat Flex3™ dressing containing AgNPs. Each sample was differently diluted (see Table 2) before injection to achieve a comparable concentration (~400 pg mL^{-1})

Conclusion

The exponentially growing market of consumer and medical products containing AgNPs has raised the urgent need for regulatory standards targeted at health and safety. Developing adequate analytical methods to achieve detection and characterization of AgNPs and their ionic counterpart in biological media is the key requisite to support regulatory requirements with robust scientific evidence.

An innovative method is proposed here for the simultaneous determination of dissolved Ag and the characterization of AgNPs in human plasma and blood. By coupling HDC separation, spICP-MS detection and a dedicated algorithm for data elaboration, comprehensive information on the chemical state of the Ag^+/AgNPs system can be retrieved in a single analytical run. While HDC separates the NPs based on their hydrodynamic diameter and spICP-MS provides information on their mass distribution, both techniques have the potential to discriminate physically and statistically (respectively) the signal of NPs from that of dissolved Ag but this advantage was not exploited before. We combined the two techniques and home-made software based on a new algorithm able to process the raw ICP-MS chromatogram for deconvoluting the signal of dissolved Ag from that of AgNPs. From a single injection, the method provides the chromatogram and concentration of dissolved Ag; the distribution of NPs in terms of hydrodynamic diameter, mass-derived diameter and size-dependent number of detected NPs; and the total number concentration and size-dependent mass concentration of the NPs. A variety of 3D chromatograms can be obtained from the results to achieve a comprehensive characterization of AgNPs.

The method is robust when applied to heavy matrices such as plasma and blood and, in principle, can be extended to other biological media and to other metallic NPs. The algorithm, in particular, is suitable for the deconvolution and determination of particulate and dissolved fractions independently by the element or just for the removal of non-stationary background in any separation technique coupled to spICP-MS.

Combining the method with μXANES speciation and imaging provides an integrated approach which opens the way to elucidate the dynamics of AgNPs in biological fluids or extracts in vivo under realistic conditions (real human subjects, real administered doses).

We applied this strategy to study the behaviour of AgNP standards and that of an AgNP-coated dressing incubated in human plasma and to investigate for the first time the capability of AgNPs to reach the systemic circulation after topical application to burn patients.

The results showed that partial dissolution of uncoated AgNPs takes place in plasma on an hourly time scale with nonlinear dynamics in a closed system. Chlorides and protein thiols co-participate in the process through complex temporal and spatial mechanisms, forced by kinetic factors. The early dynamics and dissolution of AgNPs are dominated by interaction with chlorides directly on their surface. Formation of a protein corona takes place in the meantime, resulting in the inhibition of further reactions with the medium, slower displacement of Ag from chlorides and final mobilization of the metal. As a whole, thiol binding is proposed as the main regulator of AgNPs dissolution in plasma and that of the systemic distribution of the metal. The analysis of the whole blood from burn patients suggested that the dynamics of AgNPs dissolution after topical administration takes place mainly in situ, most probably in the exudate, so that their potential to undergo systemic distribution in the intact form is minimal. Further studies are currently in progress to investigate the chemical speciation of Ag directly in wound tissues.

Acknowledgments The authors are grateful to the Italian Ministry of Education, University and Research for financial support through the project MIUR-FIRB number RBFR08M6W8. The European Synchrotron Radiation Facility is acknowledged for provision of beamtime at ID21. ELGA LabWater is acknowledged for providing the PURELAB Option-Q and Ultra Analytic systems, which produced the ultra-pure water used in these experiments. Francesca Benetello and Bruno Pavoni from Ca' Foscari University of Venice are acknowledged for the lyophilization of standards and samples.

Conflict of interest The authors declare that they have no competing interests.

Appendix

Characterization of the commercial AgNP standard dispersions

The morphological characterization of the mother AgNP standard dispersions was carried out by TEM using a Tecnai 12 G^2 instrument (FEI, USA). For the analysis, a 3 μL drop of each dispersion was deposited on a Formvar/carbon support on 200-mesh thick grid, let dry at room temperature and directly analyzed. The images were acquired at 120 kV high voltage and using a tungsten filament, twin optics and an Olympus side-mounted camera. The ImageJ software (National Institutes of Health, USA) was used for particle counting and shape characterization. Representative TEM images of the NP standards and a summary of their size/shape parameters are shown in Fig. 8 and reported in Table 3, respectively.

The z-potential was measured using a Zetasizer Nano (Malvern, UK) at 24 °C in DTS1070 cells pre-washed with a 60 μg mL^{-1} citrate-water solution. For the analysis, each standard suspension was sonicated for 5 min and equilibrated for 120 s in the cell, and five replicate measurements of 10 to 100 readings were acquired. The z-potential of the NP standards is also reported in Table 3.

Total mass concentration of Ag in the standards was measured by ICP-MS *previa* dissolution in HNO_3 5 % *v*/*v* and

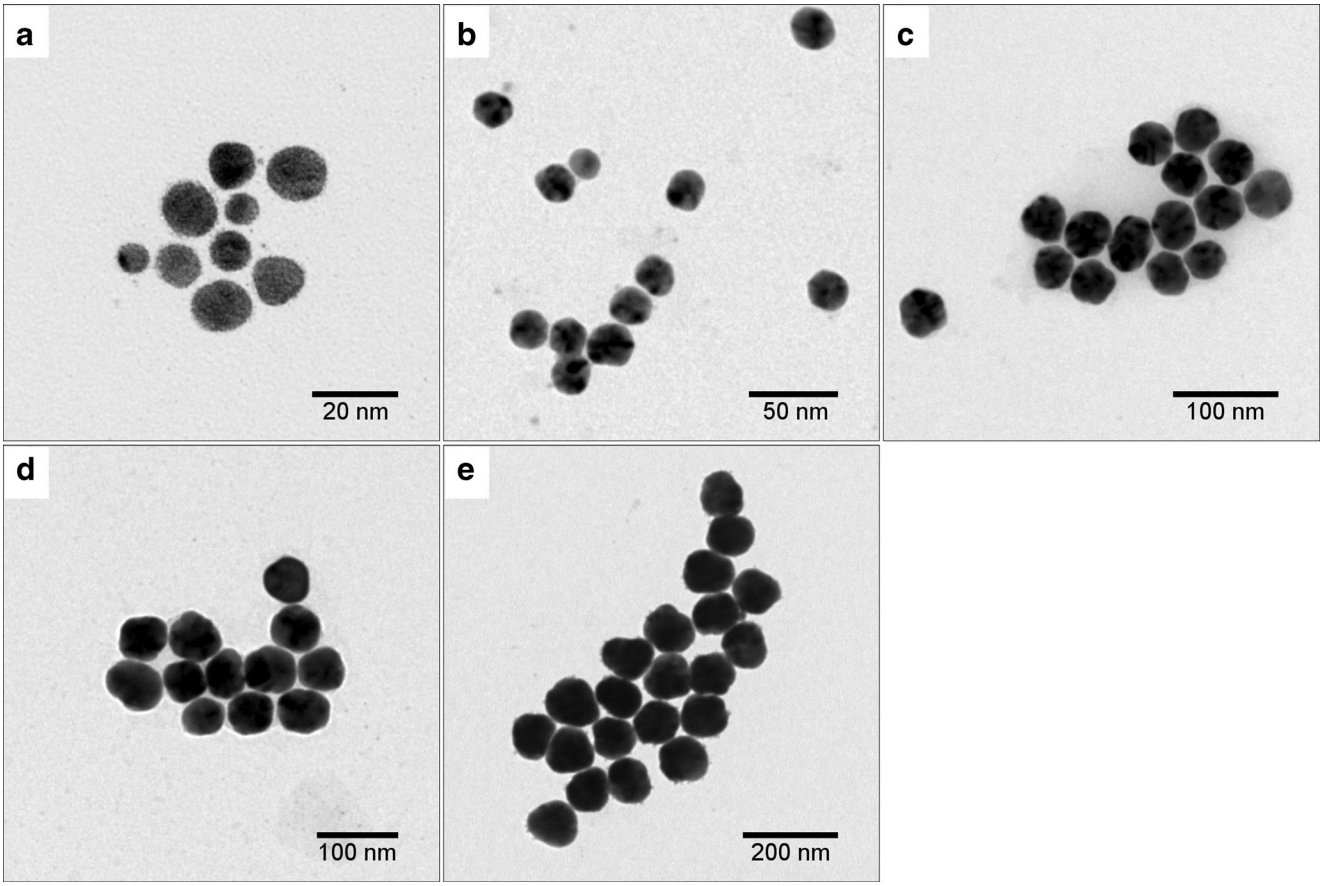

Fig. 8 TEM images of the AgNP standards (mother suspensions) used throughout the study. The nominal sizes are 10 nm (**a**), 20 nm (**b**), 40 nm (**c**), 60 nm (**d**) and 100 nm (**e**)

Table 3 Characterization of the AgNP standards (mother suspensions) used throughout the study

Nominal size±SD (nm)	Measured diameter (nm) Median (interquartile range) Average±SD Mode	Geometry Circularity±SD Roundness±SD Solidity±SD	z-potential (mV)
10±4	8.6 (7.1–10.8) 9.2±3.2 7.2	0.90±0.03 0.91±0.06 0.95±0.01	−46.4±2.2
20±4	22.2 (20.7–23.5) 21.9±2.4 23.1	0.90±0.02 0.91±0.05 0.95±0.01	−46.6±2.0
40±4	40.7 (40.2–45.1) 42.4±3.8 43.5	0.89±0.02 0.90±0.05 0.96±0.01	−45.3±1.7
60±4	56.4 (50.6–59.7) 56.5±4.5 58.7	0.89±0.02 0.89±0.06 0.96±0.01	−48.6±1.2
100±4	98.7 (95.6–102.3) 99.0±5.1 98.7	0.88±0.02 0.89±0.05 0.95±0.01	−53.2±1.4

Particles' diameter and geometry were measured by TEM on a minimum sample of 400 particles; for the z-potential, $n=5$

subsequent dilution in NH_4OH 2.8 % *w/w*. The analysis was carried out in full-quant mode by external calibration with Rh as internal standard.

Methods for μXRF and μXANES analyses

Standards and samples

Solid-state reference compounds for μXANES included the following: Ag^0 foil, AgCl, Ag_2SO_4, $AgNO_3$, Ag_2O, Ag sulfadiazine (AgSD) and a fragment of the Acticoat Flex3™ intact dressing. Reference standards of 10 and 100 nm Ag^0NPs were prepared from mother water suspensions (citrate stabilized, 20 μg mL^{-1} as Ag) by deposition of a 20 μL drop between Ultralene® windows and microscopy slides, followed by rapid freezing and freeze-drying for 24 h. A standard of Ag bonded to GSH was prepared by incubating ionic Ag (from $AgNO_3$, 10 μg mL^{-1} as Ag) in a water solution of GSH ~0.5 mg mL^{-1}, at 37 °C under gentle shaking for 2 h and in dark conditions, followed by freeze-drying as reported above. Standards of 10 nm Ag^0NPs, ionic Ag and the Acticoat Flex3™ intact dressing (2.45-mg fragment) were also incubated in a water solution containing HSA (~0.5 mg mL^{-1}) and in the whole human plasma, freeze-dried as reported above and analyzed as unknown samples.

Instrumental parameters and data elaboration

The μXRF and Ag L_{III}-edge μXANES measurements were performed using the scanning X-ray microscope of beamline ID21 at the European Synchrotron Radiation Facility (ESRF, Grenoble, France), working at room temperature conditions. Detectors included a Si_3N_7 diode for I_0 and an 80-mm active area silicon drift detector (Bruker) for the emitted fluorescence. Focusing was achieved using fixed curvature Kirkpatrick-Baez mirror optics. The photon flux was 3.6×10^9 ph s^{-1} at 3.42 keV with a beam size of 1.0×1.2 μm^2.

μXRF maps of signal intensities for individual elements (Ag, S and Cl) were collected for preliminary analysis to select optimal regions for the subsequent μXANES analysis. The μXRF maps were acquired with variable lateral resolution (0.5 to 2 μm) and integration time (100 ms). The raw data (counts) were elaborated using the PyMca software as follows: (i) correction for the settling time and conversion to counts per second (cps), (ii) deconvolution (batch fitting of the μXRF spectra) and (iii) normalization for the incident beam flux.

Batch Ag L_{III}-edge μXANES spectra of 30 s were collected and averaged for each spot of interest from 3.32 to 3.42 keV energy range with 0.5 eV steps. The beam position was slightly moved from one spectrum to another to avoid radiation damage. At least 10 spectra were averaged for each region of interest. After background removal and normalization, the spectra were calibrated by taking the first inflection point of at 3.3545 keV and then smoothed by interpolation with five iteractions. The μXANES spectra of Acticoat Flex3™ and HSA/plasma-incubated standards were treated by LCF using the Athena software with the following set of reference spectra as independent variables: Ag^0 foil, 10 nm Ag^0NPs, AgCl, Ag_2SO_4, $AgNO_2$, Ag_2O, AgSD and AgGSH. A linear term was allowed to compensate for small differences in data normalization, no energy shift was allowed, and weights and their sum were forced to sum to 1. The energy range used for fitting was 3.3345 to 3.4145 keV ($e0-0.02$ to $e0+0.06$). The quality of fitting was quantified by the normalized sum of squared residual $NSS=(\mu_{experimental}-\mu_{fit})^2/\Sigma(\mu_{experimental})^2\times100$, where μ is the normalized absorbance. Linear combinations of one, two and three reference standards were examined. The best fit with $n+1$ components was retained if NSS was decreased by more than 15 % as compared to the best fit using n components. Based on the results, four main Ag species were revealed in the samples: Ag^0 foil, 10 nm Ag^0NPs, AgCl and AgGSH; the other minority species were pooled as *other*. When two or more fits of equivalent quality (relative difference of NSS <10 %) were obtained with different combinations of such a minority species, proportions and NSS were expressed as mean percentage with standard deviation (SD) between parentheses, calculated for the equivalent fits.

The μXANES spectra were acquired in fluorescence mapping mode by scanning the beam with a 2×2 μm^2 step size and a 50 ms dwell time per pixel with 3 eV energy steps in the region from 3.320 to 3.341 KeV, 0.5 eV from 3.341 to 3.381 KeV and 1 eV from 3.382 to 3.42 KeV. This resulted in a total of 126 images recorded using a region of interest selective for Ag L3M4 and L3M5 emission lines, corrected for detector dead time (always kept below 20 %) and normalized by the incident beam flux. The stack of images was converted to an hdf5 file containing intensities and the energy values for each map to be processed using PyMca for extraction of μXANES spectra. The map was treated by moving merge of the spectra on 2×2 pixels areas and with 1 pixel step, in order to reduce the noise and improve the statistical representativity. After background removal and normalization, the spectra were calibrated and individually processed by LCF as above, but using only the reference spectra of 10 nm Ag^0NPs, AgCl and AgGSH as independent variables. Based on visual inspection of the fits, an arbitrary threshold of NSS <0.1 was adopted to remove the pixels from the map with insufficient quality of the fit. A number of pixels in the upper right side of the map (see Fig. 4b) were discarded based on this criterion. These pixels were affected by the sharp change in intensity at the border of the analyzed particle coupled to beam drift caused by scanning the energy with the double-crystal monochromator. The retained pixels were re-processed by LCF testing all combinations in which one of the three reference standards was removed. Each standard was considered

significant if its introduction decreased the NSS by more than 3 %. This threshold was calibrated a posteriori to guarantee that all pixels in the map had at least one significant component, and a coefficient equal to zero was assigned to the non-significant components. For each pixel, the coefficients were finally multiplied for the corresponding signal intensity of total Ag (from the μXRF map), also treated by the moving merge procedure, to obtain the absolute contribution of each species expressed in cps.

References

1. Rigo C, Ferroni L, Tocco I, Roman M, Munivrana I, Gardin C, Cairns WRL, Vindigni V, Azzena B, Barbante C, Zavan B (2013) Active silver nanoparticles for wound healing. Int J Mol Sci 14(3): 4817–4840
2. Wilkinson LJ, White RJ, Chipman JK (2011) Silver and nanoparticles of silver in wound dressings: a review of efficacy and safety. J Wound Care 20(11):543–549
3. Liu J, Wang Z, Liu FD, Kane AB, Hurt RH (2012) Chemical transformations of nanosilver in biological environments. ACS Nano 6(11):9887–9899
4. Reidy B, Haase A, Luch A, Dawson KA, Lynch I (2013) Mechanisms of silver nanoparticle release, transformation and toxicity: a critical review of current knowledge and recommendations for future studies and applications. Materials 6(6):2295–2350
5. Gnanadhas DP, Ben Thomas M, Thomas R, Raichur AM, Chakravortty D (2013) Interaction of silver nanoparticles with serum proteins affects their antimicrobial activity in vivo. Antimicrob Agents Chemother 57(10):4945–4955
6. Liu J, Sonshine DA, Shervani S, Hurt RH (2010) Controlled release of biologically active silver from nanosilver surfaces. ACS Nano 4(11):6903–6913
7. You CG, Han CM, Wang XG, Zheng YR, Li QY, Hu XL, Sun HF (2012) The progress of silver nanoparticles in the antibacterial mechanism, clinical application and cytotoxicity. Mol Biol Rep 39(9):9193–9201
8. Pyrz WD, Buttrey DJ (2008) Particle size determination using TEM: a discussion of image acquisition and analysis for the novice microscopist. Langmuir 24(20):11350–11360
9. Luo P, Morrison I, Dudkiewicz A, Tiede K, Boyes E, O'Toole P, Park S, Boxall AB (2013) Visualization and characterization of engineered nanoparticles in complex environmental and food matrices using atmospheric scanning electron microscopy. J Microsc 250(1):32–41
10. Grobelny J, DelRio F, Pradeep N, Kim D-I, Hackley V, Cook R (2011) Size measurement of nanoparticles using atomic force microscopy. In: McNeil SE (ed) Characterization of nanoparticles intended for drug delivery, vol 697. Methods in molecular biology. Humana, pp. 71–82. doi: 10.1007/978-1-60327-198-1_7
11. Hagendorfer H, Kaegi R, Parlinska M, Sinnet B, Ludwig C, Ulrich A (2012) Characterization of silver nanoparticle products using asymmetric flow field flow fractionation with a multidetector approach—a comparison to transmission electron microscopy and batch dynamic light scattering. Anal Chem 84(6):2678–2685
12. Proulx K, Wilkinson KJ (2014) Separation, detection and characterisation of engineered nanoparticles in natural waters using hydrodynamic chromatography and multi-method detection (light scattering, analytical ultracentrifugation and single particle ICP-MS). Environ Chem 11(4):392–401
13. Mitrano DM, Barber A, Bednar A, Westerhoff P, Higgins CP, Ranville JF (2012) Silver nanoparticle characterization using single particle ICP-MS (SP-ICP-MS) and asymmetrical flow field flow fractionation ICP-MS (AF4-ICP-MS). J Anal At Spectrom 27(7): 1131–1142
14. Wimuktiwan P, Shiowatana J, Siripinyanond A (2015) Investigation of silver nanoparticles and plasma protein association using flow field-flow fractionation coupled with inductively coupled plasma mass spectrometry (FlFFF-ICP-MS). J Anal At Spectrom 30(1):245–253
15. Ramos K, Ramos L, Camara C, Gomez-Gomez MM (2014) Characterization and quantification of silver nanoparticles in nutraceuticals and beverages by asymmetric flow field flow fractionation coupled with inductively coupled plasma mass spectrometry. J Chromatogr 1371:227–236
16. Philippe A, Gangloff M, Rakcheev D, Schaumann GE (2014) Evaluation of hydrodynamic chromatography coupled with inductively coupled plasma mass spectrometry detector for analysis of colloids in environmental media—effects of colloid composition, coating and shape. Anal Methods 6(21):8722–8728
17. Lewis DJ (2015) Hydrodynamic chromatography-inductively coupled plasma mass spectrometry, with post-column injection capability for simultaneous determination of nanoparticle size, mass concentration and particle number concentration (HDC-PCi-ICP-MS). Analyst 140(5):1624–1628
18. Soto-Alvaredo J, Montes-Bayon M, Bettmer J (2013) Speciation of silver nanoparticles and silver(I) by reversed-phase liquid chromatography coupled to ICPMS. Anal Chem 85(3):1316–1321
19. Franze B, Engelhard C (2014) Fast separation, characterization, and speciation of gold and silver nanoparticles and their ionic counterparts with micellar electrokinetic chromatography coupled to ICP-MS. Anal Chem 86(12):5713–5720
20. Laborda F, Bolea E, Jimenez-Lamana J (2014) Single particle inductively coupled plasma mass spectrometry: a powerful tool for nanoanalysis. Anal Chem 86(5):2270–2278
21. Yang Y, Long CL, Yang ZG, Li HP, Wang Q (2014) Characterization and determination of silver nanoparticle using single particle-inductively coupled plasma-mass spectrometry. Chin J Anal Chem 42(11):1553–1559
22. Lee S, Bi XY, Reed RB, Ranville JF, Herckes P, Westerhoff P (2014) Nanoparticle size detection limits by single particle ICP-MS for 40 elements. Environ Sci Technol 48(17):10291–10300
23. Mitrano DM, Ranville JF, Bednar A, Kazor K, Hering AS, Higgins CP (2014) Tracking dissolution of silver nanoparticles at environmentally relevant concentrations in laboratory, natural, and processed waters using single particle ICP-MS (spICP-MS). Environ Sci Nano 1(3):248–259
24. Furtado LM, Hoque ME, Mitrano DF, Ranville JF, Cheever B, Frost PC, Xenopoulos MA, Hintelmann H, Metcalfe CD (2014) The persistence and transformation of silver nanoparticles in littoral lake mesocosms monitored using various analytical techniques. Environ Chem 11(4):419–430
25. Mitrano DM, Lesher EK, Bednar A, Monserud J, Higgins CP, Ranville JF (2012) Detecting nanoparticulate silver using single-particle inductively coupled plasma-mass spectrometry. Environ Toxicol Chem 31(1):115–121
26. Peters RJB, Rivera ZH, van Bemmel G, Marvin HJP, Weigel S, Bouwmeester H (2014) Development and validation of single particle ICP-MS for sizing and quantitative determination of nanosilver in chicken meat. Anal Bioanal Chem 406(16):3875–3885
27. Loeschner K, Navratilova J, Kobler C, Molhave K, Wagner S, von der Kammer F, Larsen EH (2013) Detection and characterization of silver nanoparticles in chicken meat by asymmetric flow field flow fractionation with detection by conventional or single particle ICP-MS. Anal Bioanal Chem 405(25):8185–8195

28. Pergantis SA, Jones-Lepp TL, Heithmar EM (2012) Hydrodynamic chromatography online with single particle-inductively coupled plasma mass spectrometry for ultratrace detection of metal-containing nanoparticles. Anal Chem 84(15):6454–6462
29. Grombe R, Allmaier G, Charoud-Got J, Dudkiewicz A, Emteborg H, Hofmann T, Larsen EH, Lehner A, Llinas M, Loeschner K, Molhave K, Peters RJ, Seghers J, Solans C, von der Kammer F, Wagner S, Weigel S, Linsinger TPJ (2015) Feasibility of the development of reference materials for the detection of Ag nanoparticles in food: neat dispersions and spiked chicken meat. Accred Qual Assur 20(1):3–16
30. Liu JY, Murphy KE, MacCuspie RI, Winchester MR (2014) Capabilities of single particle inductively coupled plasma mass spectrometry for the size measurement of nanoparticles: a case study on gold nanoparticles. Anal Chem 86(7):3405–3414
31. Cornelis G, Hassellov M (2014) A signal deconvolution method to discriminate smaller nanoparticles in single particle ICP-MS. J Anal At Spectrom 29(1):134–144
32. Roman M, Rigo C, Munivrana I, Vindigni V, Azzena B, Barbante C, Fenzi F, Guerriero P, Cairns WRL (2013) Development and application of methods for the determination of silver in polymeric dressings used for the care of burns. Talanta 115:94–103
33. Solé VA, Papillon E, Cotte M, Walter P, Susini J (2007) A multiplatform code for the analysis of energy-dispersive X-ray fluorescence spectra. Spectrochim Acta B 62(1):63–68
34. Ravel B, Newville M (2005) ATHENA, ARTEMIS, HEPHAESTUS: data analysis for X-ray absorption spectroscopy using IFEFFIT. J Synchrotron Radiat 12(4):537–541
35. Tuoriniemi J, Cornelis G, Hassellov M (2014) Improving the accuracy of single particle ICPMS for measurement of size distributions and number concentrations of nanoparticles by determining analyte partitioning during nebulisation. J Anal At Spectrom 29(4): 743–752
36. Montano MD, Badiei HR, Bazargan S, Ranville JF (2014) Improvements in the detection and characterization of engineered nanoparticles using spICP-MS with microsecond dwell times. Environ Sci Nano 1(4):338–346
37. Hineman A, Stephan C (2014) Effect of dwell time on single particle inductively coupled plasma mass spectrometry data acquisition quality. J Anal At Spectrom 29(7):1252–1257
38. Pace HE, Rogers NJ, Jarolimek C, Coleman VA, Higgins CP, Ranville JF (2011) Determining transport efficiency for the purpose of counting and sizing nanoparticles via single particle inductively coupled plasma mass spectrometry. Anal Chem 83(24):9361–9369
39. Cedervall T, Lynch I, Lindman S, Berggard T, Thulin E, Nilsson H, Dawson KA, Linse S (2007) Understanding the nanoparticle-protein corona using methods to quantify exchange rates and affinities of proteins for nanoparticles. Proc Natl Acad Sci U S A 104(7): 2050–2055
40. Shannahan JH, Lai XY, Ke PC, Podila R, Brown JM, Witzmann FA (2013) Silver nanoparticle protein corona composition in cell culture media. PLoS One 8(9)
41. Rigo C, Roman M, Munivrana I, Vindigni V, Azzena B, Barbante C, Cairns WRL (2012) Characterization and evaluation of silver release from four different dressings used in burns care. Burns 38(8):1131–1142
42. Adams NWH, Kramer JR (1999) Silver speciation in wastewater effluent, surface waters, and pore waters. Environ Toxicol Chem 18(12):2667–2673
43. Larese FF, D'Agostin F, Crosera M, Adami G, Renzi N, Bovenzi M, Maina G (2009) Human skin penetration of silver nanoparticles through intact and damaged skin. Toxicology 255(1–2):33–37
44. Armitage SA, White MA, Wilson HK (1996) The determination of silver in whole blood and its application to biological monitoring of occupationally exposed groups. Ann Occup Hyg 40(3):331–338
45. Wang XQ, Kempf M, Mott J, Chang HE, Francis R, Liu PY, Cuttle L, Olszowy H, Kravchuk O, Mill J, Kimble RM (2009) Silver absorption on burns after the application of Acticoat(TM): data from pediatric patients and a porcine burn model. J Burn Care Res 30(2):341–348
46. Schneider L, Korber A, Grabbe S, Dissemond J (2007) Influence of pH on wound-healing: a new perspective for wound-therapy? Arch Dermatol Res 298(9):413–420